

RESEARCH ARTICLE

Moth eye-inspired highly efficient, robust, and neutral-colored semitransparent perovskite solar cells for building-integrated photovoltaics

Yiyi Zhu^{1,2} | Lei Shu^{1,2} | Qianpeng Zhang^{1,2} | Yudong Zhu^{1,3} | Swapnadeep Poddar^{1,2} | Chen Wang^{1,2} | Zhubing He³ | Zhiyong Fan^{1,2,4} 

¹Department of Electronic & Computer Engineering, The Hong Kong University of Science and Technology, Clear Water Bay, Kowloon, Hong Kong

²HKUST-Shenzhen Research Institute, Shenzhen, China

³Department of Materials Science and Engineering, Shenzhen Key Laboratory of Full Spectral Solar Electricity Generation (FSSEG), Southern University of Science and Technology, Shenzhen, China

⁴Guangdong-Hong Kong-Macao Joint Laboratory for Intelligent Micro-Nano Optoelectronic Technology, HKUST, Clear Water Bay, Kowloon, Hong Kong

Correspondence

Zhiyong Fan, Department of Electronic & Computer Engineering, The Hong Kong University of Science and Technology, Clear Water Bay, Kowloon, Hong Kong SAR, China.

Email: eezfan@ust.hk

Funding information

the Science and Technology Plan of Shenzhen, Grant/Award Numbers: JCYJ20170818114107730, JCYJ20180306174923335; Guangdong-Hong Kong-Macao Intelligent Micro-Nano Optoelectronic Technology Joint Laboratory, Grant/Award Number: 2020B1212030010; HKUST Fund of Nanhai, Grant/Award Number: FSNH-18FYTRI01; National Natural Science Foundation of China, Grant/Award Number: 51672231; the Center for 1D/2D Quantum Materials and the State Key Laboratory of Advanced Displays and Optoelectronics Technologies at HKUST and Foshan Innovative and Entrepreneurial Research Team Program, Grant/Award Number: 2018IT100031; the General Research Fund from the Hong Kong Research Grant Council, Grant/Award Numbers: 16214619, 16309018

Abstract

Semi-transparent perovskite solar cells (ST-PSCs) engendered enormous attention for practical applications such as power generation windows. However, it is still challenging to achieve high-performance, robust and neutral-colored ST-PSCs. Herein we demonstrate a moth-eye-inspired structure (MEIS) for light-trapping photons in the wavelength range where the human eye is less perceptive. This biomimetic structure contributes to the improvements in ST-PSCs performance and visual appearance simultaneously. Consequently, a record high figure-of-merit for ST-PSC, defined as the product of power conversion efficiency and the average visible transmittance, is achieved. Meanwhile, the optical appearance is converted to a desired near-neutral color after introducing the MEIS. The investigation of ST-PSCs with long-term stability is implemented via engineering blend ratio of halides. The modified device exhibited appealing tolerance against moisture and solar irradiation. This work reveals an in-depth understanding of light trapping along with modifying the visual appearance of solar cells.

KEYWORDS

building-integrated photovoltaics, human luminosity, moth-eye, perovskites, semitransparent solar cell

This is an open access article under the terms of the Creative Commons Attribution License, which permits use, distribution and reproduction in any medium, provided the original work is properly cited.

© 2021 The Authors. *EcoMat* published by The Hong Kong Polytechnic University and John Wiley & Sons Australia, Ltd.

1 | INTRODUCTION

The power consumption of buildings is tremendous.¹ Moreover, a vast amount of energy is wasted during distribution. For instance in the United States, 25 TWh of electricity is consumed by buildings each year, accounting for nearly 40% of the total energy demand.² Researchers are exploring solutions to this issue. Currently, traditional solar panels are opaque and can only be mounted in the limited space of rooftops. In modern densely packed cities, a more efficient utilization of solar energy is the need of the hour. One of the feasible solutions is to install semitransparent solar panels onto the windows, facades, and skylights.²⁻⁴

The emerging semi-transparent perovskite solar cells (ST-PSCs) have gradually come to the fore for building-integrated photovoltaics (BIPV).⁵ Particularly in the application for power generation windows, ST-PSCs must harvest sunlight and convert it to electricity while transmitting part of daylight to illuminate indoor space. Besides efficiency, which is the primary figure-of-merit for most photovoltaic devices, attributes such as average visible transmittance (AVT), color, and longevity are also key specifications for ST-PSCs. The AVT can be modified by tuning the perovskite thickness or surface coverage.^{6,7} Generally, an AVT of 20%–30% can satisfy the transmittance requirement of power-generating windows.⁷ The conventional structure for ST-PSCs requires continuous ultrathin perovskites; nevertheless, one of its limitations is the undesired hue of reddish-brown.⁸⁻¹⁵

Eperon et al. attempted to reduce perovskite surface coverage and attained neutral-colored ST-PSCs.^{16,17} But this strategy rendered low efficiency, with a 3.5% power conversion efficiency (PCE) achieved at AVT 30%. The loss of PCE can be ascribed to the shunt current from the direct contact of the electron transport layer (ETL) with the hole transport layer (HTL).¹⁸ Besides, the non-uniform surface coverage resulted in unfavorable scattering.

Apart from the intrinsic optical properties of materials, colors are also determined by the surface architectures.¹⁹⁻²³ For instance, the moth-eye surface is covered by hexagonally closely packed microcavities, which is one of the intriguing photonic structures invented by mother nature (Figure 1A).²⁴ This evolutionary advancement provides moth night vision capability and other unique functions. Notably, the MEIS is a broadband anti-reflecting layer,^{25,26} and its surface geometry offers a possibility to alter reflection spectra and optical appearance.²⁷⁻²⁹ Additionally, human visual perception is different to photons at a different wavelength.³⁰ Thus, harvesting solar radiation in the low responsive regions is a logical approach toward a highly visual-transparent and efficient ST-PSCs which the incorporation of MEIS realized.³⁰

To achieve efficient light-harvesting in the desired wavelength range, herein, we report a biomimetic MEIS ST-PSCs. The MEIS demonstrates an appealing light manipulation, which benefits the light-harvesting in the wavelength range where the human eye is less sensitive. As a result, the PCE of MEIS-based devices is significantly improved without compromise AVT. Moreover, due to the alteration of the absorption spectra, a desired near-neutral color is achieved in MEIS based device. Besides, the perovskites with robust performance were investigated in this work.

2 | RESULTS AND DISCUSSION

Figure 1A shows a schematic device structure of MEIS ST-PSCs. Figure 1B shows the fabrication process of the device. Briefly, the polystyrene (PS) spheres are assembled on planar-ITO using the Langmuir–Blodgett technique, which is a template used to pattern MEIS-ITO. Then PS spheres are covered with ITO by sputtering. Next, the PS spheres are removed, and the biomimetic MEIS-ITO is obtained.

Thereafter, SnO₂ is deposited on top through the atomic layer deposition (ALD), followed by a one-step spin-coating of perovskite and 2,2',7,7'-Tetrakis[*N,N*-di(4-methoxyphenyl)amino]-9,9'-spirobifluorene (spiro-OMeTAD). Finally, a buffer layer of MoO₃ is evaporated, followed by sputtering of indium zinc oxide (IZO) as a top electrode. In-depth experimental details can be found in the Section 3.

The tilted-angle view and top view scanning electron microscopy (SEM) images of as-assembled PS spheres and MEIS-ITO are shown in Figure 1C1, C2, D1, D2, respectively. The PS spheres, with a diameter of 900–950 nm, are uniformly distributed on the ITO. The distance of two neighboring spheres is 50–100 nm. The hexagonally arranged MEIS shows a depth of 250 nm and a diameter of 900–950 nm. The cross-sectional SEM image of the whole device based on MEIS and planar counterpart is shown in Figures 1E and S1A, respectively. Figure 1E confirms a conformal and uniform coverage of SnO₂ on MEIS-ITO with a controlled thickness. Close contact is formed at the interface between perovskite and SnO₂. Although similar MEIS structures were reported in a few works fabricated with solution methods,^{18,31} obtaining a crack-free MEIS structure has been a challenge. The presence of cracks is detrimental to a cell. Because these regions with a direct perovskites/electrode contact may result in a short circuit due to the wretched hole blocking.^{32,33} To address this bottleneck challenge described in previous reports, we utilized the sputtering of ITO for the first time to form the crack-free MEIS structure.

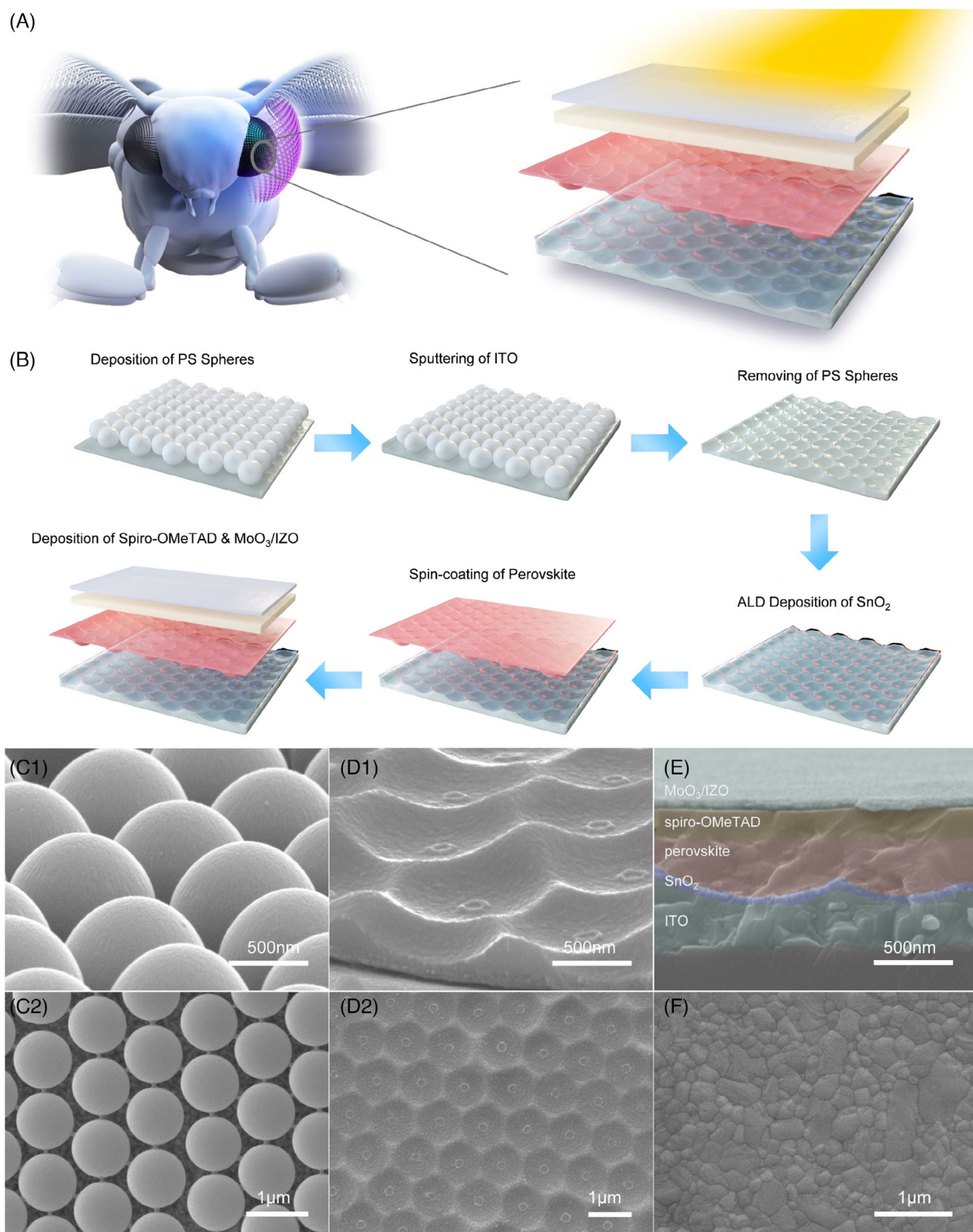


FIGURE 1 (A) Complete compound moth eyes and the moth-eye-inspired structure (MEIS) device structure diagram. (B) Schematic illustration of the fabrication procedure for the MEIS ST-PSCs. (C1) The tilted-view and (C2) top-view SEM images of PS spheres on ITO. (D1) The tilted-view and (D2) top-view SEM images of MEIS-ITO. (E) Cross-sectional SEM image of the whole device based on MEIS, and (F) top-view SEM of perovskites on the SnO₂/MEIS-ITO

Additionally, the micro-scale MEIS-ITO offers a possibility to achieve patterned high-crystallinity perovskites. Revealed in Figures 1F and S1B, compact and single-crystalline $\text{Cs}_{0.05}\text{FA}_{0.83}\text{MA}_{0.12}\text{PbBr}_{0.33}\text{I}_{2.67}$ with grain size as large as $1\ \mu\text{m}$ is acquired. Shown in Figures 1E and S1B, the patterned perovskite is compact, rendering the grain boundaries hard to discern. As most perovskite boundaries are perpendicular to the substrate, the undesired impacts of defects at the grain boundaries are minimized.^{34,35}

As shown in Figure 2A, all the XRD patterns match well with the cubic phase perovskites (Space-group: $\text{Pm}\bar{3}\text{m}$, $\alpha = 90^\circ$). The miller indices (hkl) and peak position (2θ) are listed in Table S1. No impurity diffraction peak is observed. With the increase of Br concentration (from $x = 0$ to $x = 0.46$), a peak position shift is observed, reflected from the 2θ of (100) from 14.032° to 14.096° . The lattice constant and full-width half maximum (FWHM) are listed in Table S2. The FWHM of the

(100) plane shows no noticeable change. This means Br incorporation does not play a vital role in controlling grain size, further confirmed in the top-view SEM (Figure S1). Figures 2B and S2 show the steady-state photoluminescence (PL) spectra and absorbance spectra of $\text{Cs}_{0.05}\text{FA}_{0.83}\text{MA}_{0.12}\text{PbBr}_x\text{I}_{3-x}$ on quartz, respectively. The PL emission is blue-shifted with the enhancement of Br incorporation. The lattice constant and bandgap both vary linearly with the increase of Br concentration, suggesting that the variation precisely follows Vegard's law³⁶ and a solid solution of the I/Br mixtures are formed (Figure S3). The complex refractive index spectra (n , k) of $\text{Cs}_{0.05}\text{FA}_{0.83}\text{MA}_{0.12}\text{PbBr}_{0.333}\text{I}_{2.667}$ is plotted in Figure 2C. The real part n value lies in the range from 2.1 to 2.4 in the wavelength range from 400 to 900 nm. The imaginary part k is the extinction coefficient consistent with the measured absorbance spectra (Figure S2). The original data and more discussion can be found in Figure S4.

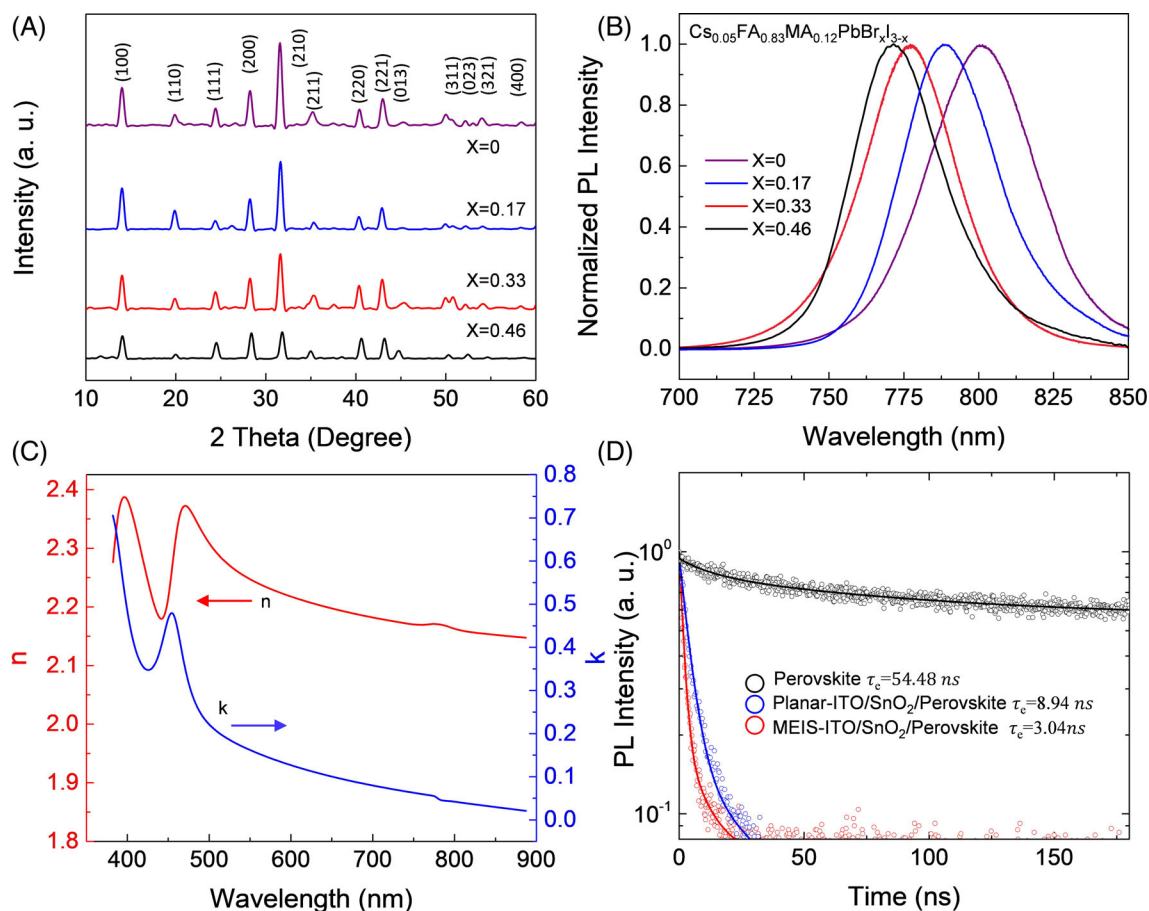


FIGURE 2 (A) X-ray diffraction patterns of (from bottom to top) MEIS-ITO/ SnO_2 / $\text{Cs}_{0.05}\text{FA}_{0.83}\text{MA}_{0.12}\text{PbBr}_x\text{I}_{3-x}$. (B) The steady-state photoluminescence (PL) spectra of $\text{Cs}_{0.05}\text{FA}_{0.83}\text{MA}_{0.12}\text{PbBr}_x\text{I}_{3-x}$ on quartz. The PL spectra are obtained with 600 nm excitation. (C) Real n and imaginary k parts of the refractive index of $\text{Cs}_{0.05}\text{FA}_{0.83}\text{MA}_{0.12}\text{PbBr}_{0.333}\text{I}_{2.667}$ calculated from the ellipsometer at room temperature. (D) Time-resolved photoluminescence (TRPL) analysis of $\text{Cs}_{0.05}\text{FA}_{0.83}\text{MA}_{0.12}\text{PbBr}_{0.33}\text{I}_{2.67}$ with and without an electron quencher (SnO_2 / planar-ITO and SnO_2 /MEIS-ITO), along with extracted exponential fits to the decay curves

The carrier lifetime of perovskites and the charge injection from the perovskites to electron quenchers are investigated through the time-resolved photoluminescence analysis (TRPL). The TRPL measurements Figure 2D reveals a lifetime of $\tau_e = 54.48$ ns for the neat $\text{Cs}_{0.05}\text{FA}_{0.83}\text{MA}_{0.12}\text{PbBr}_{0.33}\text{I}_{2.67}$, where τ_e is the time taken for the PL to plummet to $1/e$ of its initial intensity.^{37,38} The quenching samples were prepared by one-step spinning coating deposition of $\text{Cs}_{0.05}\text{FA}_{0.83}\text{MA}_{0.12}\text{PbBr}_{0.33}\text{I}_{2.67}$ on $\text{SnO}_2/\text{planar-ITO}$ and $\text{SnO}_2/\text{MEIS-ITO}$, respectively. A substantial quenching is observed in $\text{Cs}_{0.05}\text{FA}_{0.83}\text{MA}_{0.12}\text{PbBr}_{0.33}\text{I}_{2.67}$ on $\text{SnO}_2/\text{planar-ITO}$ reducing the lifetime to $\tau_e = 8.94$ ns. This is further shorted to $\tau_e = 3.04$ ns for $\text{Cs}_{0.05}\text{FA}_{0.83}\text{MA}_{0.12}\text{PbBr}_{0.33}\text{I}_{2.67}$ on $\text{SnO}_2/\text{MEIS-ITO}$. Improved PL quenching bears evidence that MEIS facilitates a more efficient carrier separation and collection at the interface than the planar counterpart.

The device optical property is investigated in this work. Figure 3A shows the reflection spectra of $\text{SnO}_2/\text{MEIS-ITO}$ and the human luminosity curve. Human eyes are sensitive to green light but less responsive to the

photon in the blue and red regions.³⁹ Owing to the MEIS geometry-assisted light-manipulation, the $\text{SnO}_2/\text{MEIS-ITO}$ manifests a unique broadband anti-reflection mimicking the moth-eye.^{25,28,29} Notably, the reflection spectra of our $\text{SnO}_2/\text{MEIS-ITO}$ precisely matches well with the human luminosity curve. This is further resolved in the transmission and absorption spectra (Figure S5) and photographs of $\text{SnO}_2/\text{MEIS-ITO}$ (the inset in Figure 3A). Even though MEIS-ITO is well-designed for ST-PSCs, the geometry still possesses variation (Figure S6), and the reflection spectra will be altered along with the modification of MEIS geometry (Figure S7).

Figure 3B is the plotted color coordinates of $\text{Cs}_{0.05}\text{FA}_{0.83}\text{MA}_{0.12}\text{PbBr}_{x}\text{I}_{3-x}$ on $\text{SnO}_2/\text{planar-ITO}$, $\text{SnO}_2/\text{MEIS-ITO}$ under AM1.5 illumination, on the CIE xy 1931 chromaticity diagram. The original data are listed in Table S3. The MEIS contributes to improved optical appearance, especially for perovskites with a high-level Br doping ($x = 0.33, 0.46$). For instance, the color coordinates (x, y) of $\text{Cs}_{0.05}\text{FA}_{0.83}\text{MA}_{0.12}\text{PbBr}_{0.33}\text{I}_{2.67}$ varies from (0.396, 0.396) for planar to (0.366, 0.344) for MEIS device.

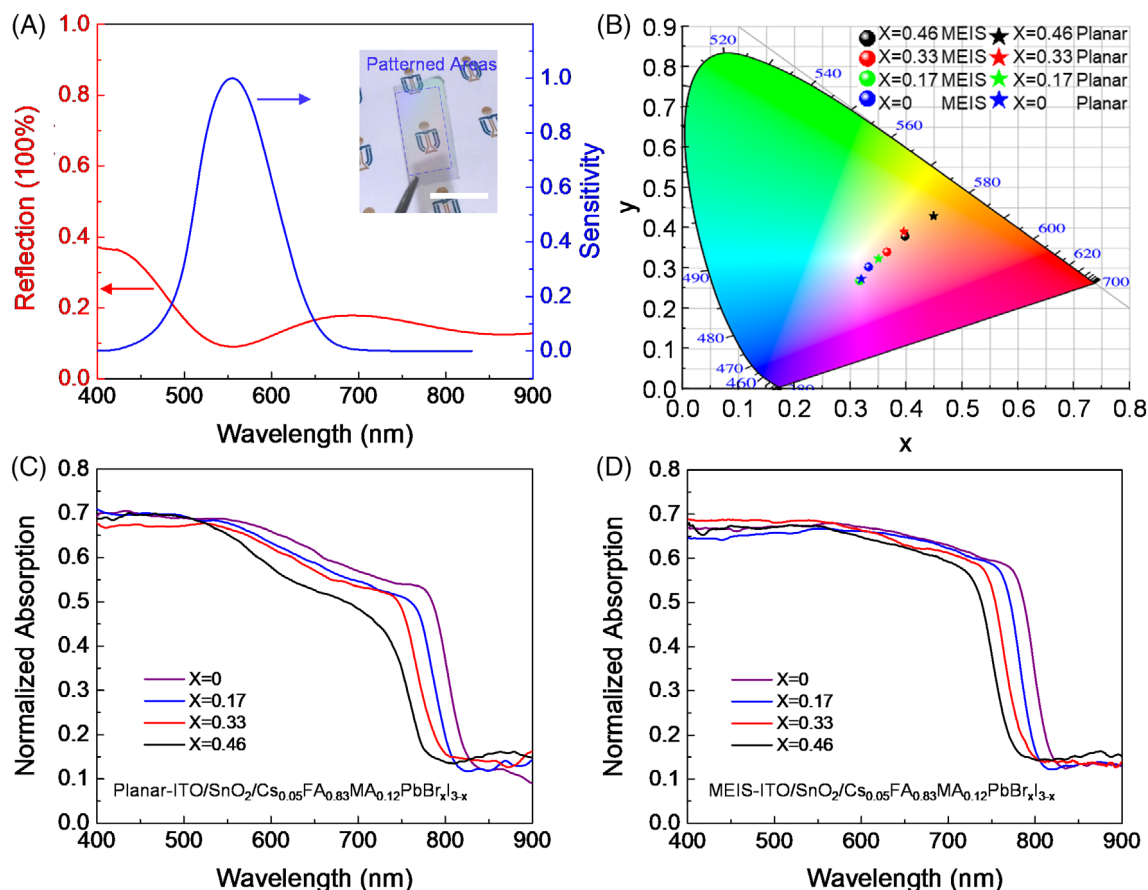


FIGURE 3 (A) Reflectance spectra of $\text{SnO}_2/\text{MEIS-ITO}$ and human luminosity curve, the inset is the photograph of $\text{SnO}_2/\text{MEIS-ITO}$ taken under AM1.5 illumination (scale bars, 3 cm). (B) Color coordinates of the films with absorption spectra shown in (C, D), under AM1.5 illumination, on the CIE xy 1931 chromaticity diagram. The UV-vis absorption spectra of $\text{Cs}_{0.05}\text{FA}_{0.83}\text{MA}_{0.12}\text{PbBr}_{x}\text{I}_{3-x}$ on $\text{SnO}_2/\text{planar-ITO}$ (C) and $\text{SnO}_2/\text{MEIS-ITO}$ (D), respectively [Correction added on 30 June 2021, after first online publication: Figures 3A and 3B have been corrected.]

The photographs (Figure 4D) further affirm this color perception management. Even though the perovskites with a low Br concentration ($x = 0, 0.17$) show desired color-neutrality, the aging test demonstrated that longevity would significantly decrease by reducing Br concentration.

We further investigated the impact of MEIS-ITO on the absorption spectrum of perovskites. The corresponding Tauc plot is shown in Figure S8. As revealed in Figure 3C, the absorption of $\text{Cs}_{0.05}\text{FA}_{0.83}\text{MA}_{0.12}\text{PbBr}_{x-3-x}$ on $\text{SnO}_2/\text{planar-ITO}$ increases monotonically from the bandgap. This can be ascribed to the trap states near the conduction band minimum (CBM) and valence band maximum (VBM) in the ultra-thin polycrystalline perovskite. The loss of the light absorption in the red region is the cause for the undesired reddish-brown hue of the ultra-thin perovskite. Besides, a steeper slope is observed in the absorption spectra as the Br doping reaches the point of $x = 0.46$, attributed to crystalline structure breakage caused by the excess amount of Br.⁴⁰ In Figure 3D, compared with the planar

counterpart, there is enhanced broadband absorption of perovskites on $\text{SnO}_2/\text{MEIS-ITO}$, especially for the longer-wavelength photons.^{41–43} MEIS shape are used in the back to couple the photons into the perovskites and thereby enhance the absorption without compromising AVT.⁴⁴ Most photons (400–500 nm) are absorbed in the single path of perovskites, making the light-coupling effect of these wavelengths less observable. In contrast, a boosted light-harvesting is witnessed for the photons at the wavelength of 600–800 nm. The photons at these wavelengths are less absorbed in a single path. The light-coupling increases the optical length in perovskites and enhances the light-harvesting of these wavelengths, consequently. The unique optical property of MEIS results in the alteration of visual appearance to the near color-neutrality as illustrated in color coordinates Figure 3B and the photograph of device Figure 4D. This result is further confirmed by the finite-difference time-domain (FDTD) simulations (Figure S9).

The photovoltaic devices with $\text{ITO}/\text{SnO}_2/\text{Cs}_{0.05}\text{FA}_{0.83}\text{MA}_{0.12}\text{PbBr}_{x-3-x}/\text{spiro-OMeTAD}/\text{MoO}_3/\text{IZO}$ structure is

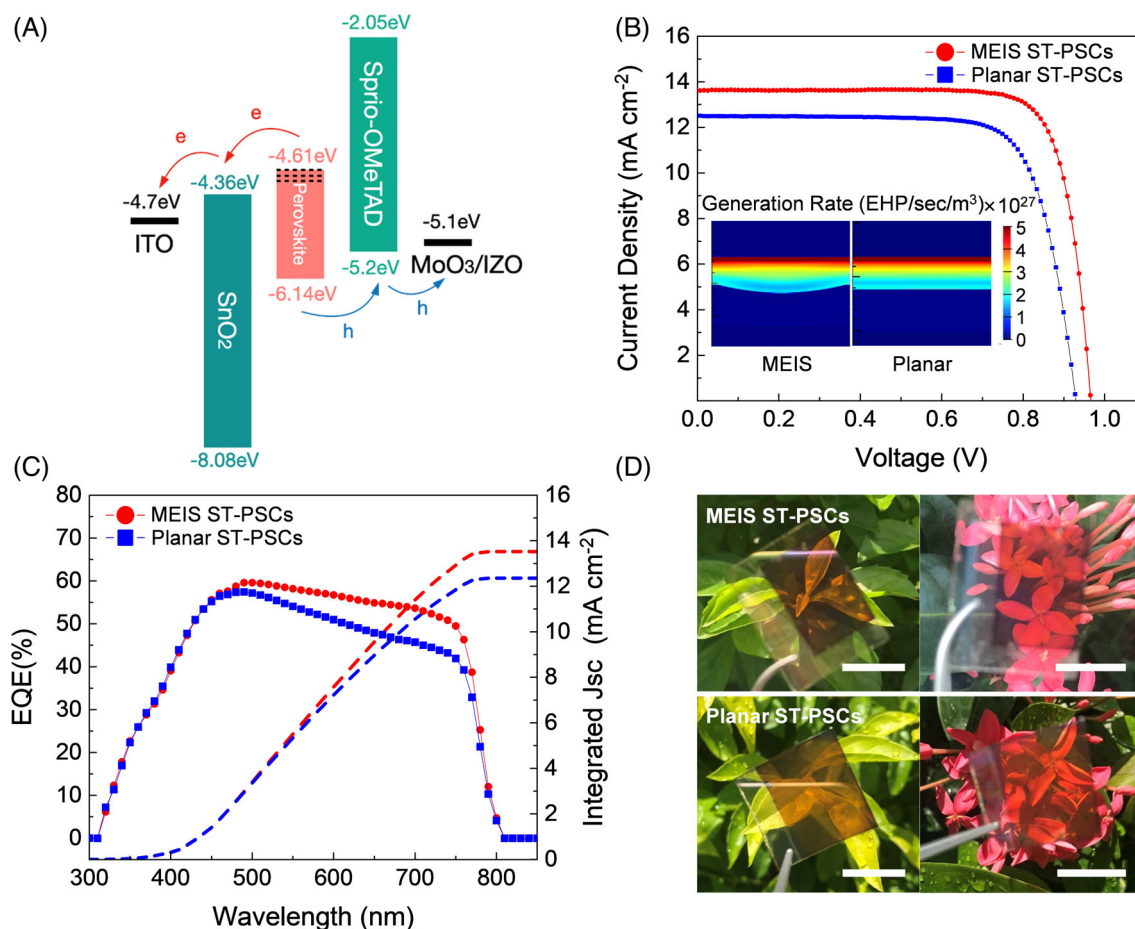


FIGURE 4 (A) Band-energy diagram of the complete device. (B) J - V curves of the champion planar and MEIS ST-PSCs based on $\text{Cs}_{0.05}\text{FA}_{0.83}\text{MA}_{0.12}\text{PbBr}_{0.33}\text{I}_{2.67}$ under simulated AM1.5G illumination, with an active area of $\sim 0.03 \text{ cm}^2$, the inset is the simulated photocarrier generation rates ($\text{EHP}/\text{sec}/\text{m}^3$) of (B). (C) External quantum efficiency (EQE) of (B). The integrated product of the EQE spectra with the AM1.5G photon flux is also shown (dash lines). (D) The photographs of (B), taken under outdoor sunlight (scale bars, 2 cm)

fabricated. Figure 4A shows the energy-band diagram of the complete device. Band energy levels of SnO_2 ,⁴⁵ spiro-OMeTAD,⁴⁶ MoO_3/IZO ⁴⁷ are obtained from previously published literature. The VBM of $\text{Cs}_{0.05}\text{FA}_{0.83}\text{MA}_{0.125}\text{PbBr}_x\text{I}_{3-x}$ is -6.14 eV, derived by ultraviolet photoelectron spectroscopy (UPS) measurement (Figure S10), whereas the CBM is obtained by combining VBM with optical bandgap (Figure S8). The CBM of $\text{Cs}_{0.05}\text{FA}_{0.83}\text{MA}_{0.12}\text{PbBr}_x\text{I}_{3-x}$ ($x = 0, 0.17, 0.33, 0.46$) is estimated to be $-4.52, -4.55, -4.58,$ and -4.61 eV, respectively. The $\text{Cs}_{0.05}\text{FA}_{0.83}\text{MA}_{0.125}\text{PbBr}_x\text{I}_{3-x}$ all demonstrate a proper energy level alignment with SnO_2 and spiro-MeOTAD.

Figure 4B shows the current density-voltage (J - V) curves based on $\text{Cs}_{0.05}\text{FA}_{0.83}\text{MA}_{0.12}\text{PbBr}_{0.33}\text{I}_{0.27}$ for planar and MEIS devices. The planar counterpart yielded a PCE of 8.78% at AVT of 35.00% with a short-circuit current density (J_{sc}) of 12.51 mA cm^{-2} , an open-circuit voltage (V_{oc}) of 0.93 V and a fill factor (FF) of 75.47%. Intriguingly, the MEIS device elevated the PCE to 10.53% ($V_{\text{oc}} = 0.97 \text{ V}$, $J_{\text{sc}} = 13.65 \text{ mA cm}^{-2}$, $\text{FF} = 79.60\%$) at AVT of 32.50%. The inset of Figure 4B shows the simulated photo-carriers generation rates (EHP/sec/ m^3) on the fabricated ST-PSCs. The MEIS structure has less perovskite materials, however showing higher absorption (Figure S9) compared to the planar counterpart. As revealed in Figure 4C, a higher external quantum efficiency (EQE) in the red region is observed in the MEIS device, producing an enhanced integrated current density of 13.52 mA cm^{-2} for MEIS compared with the planar counterpart (12.36 mA cm^{-2}). Figure 4D are photographs of the planar and MEIS devices based on $\text{Cs}_{0.05}\text{FA}_{0.83}\text{MA}_{0.12}\text{PbBr}_{0.33}\text{I}_{0.27}$, taken under outdoor sunlight. The device based on planar and MEIS both demonstrate high visual transparency. Compared with the reddish-brown hue of the planar device, a preferred near-color-neutrality was obtained in

the MEIS device. In addition, the incident angle of sunlight varies over time, the angular-dependent performance of a solar cell is a concern for its real application.⁴⁸⁻⁵⁰ Shown in Figure S11, in contrast to the planar counterpart, the MEIS ST-PSCs possess an appealing capability of harvesting photons from a wide angle with a broad wavelength range.

Figure 5A shows the J - V curves of MEIS ST-PSCs with different Br concentrations. The AVT and luminosity of devices are listed in Table S5. The level of Br doping does not affect the efficiency dramatically, and J_{sc} is only slightly decreased with the increase of Br concentration in perovskite. Whereas the degree of Br incorporation remarkably impacts long-term stability which are major concerns for practical applications.

In Figure 5B, we performed a long-term stability test on the devices by placing the unencapsulated MEIS ST-PSCs in a desiccator with humidity below 10% and tested in an ambient environment 70%–90% humidity every week. Moisture tolerance is observed in the device based on $\text{Cs}_{0.05}\text{FA}_{0.83}\text{MA}_{0.12}\text{PbBr}_{0.33}\text{I}_{0.27}$, as the unpackaged device retained above 80% of its original PCE after 224 days. In contrast, the device based on $\text{Cs}_{0.05}\text{FA}_{0.83}\text{MA}_{0.12}\text{PbBr}_x\text{I}_{3-x}$ with a low Br concentration ($x = 0, 0.17$) decomposed within 20 min when exposed at ambient conditions (humidity = 70%–90%). To further ascertain the photostability, we implemented a light-soaking stability test by exposure the encapsulated device based on $\text{Cs}_{0.05}\text{FA}_{0.83}\text{MA}_{0.12}\text{PbBr}_{0.33}\text{I}_{0.27}$ under continuous AM1.5G illumination in the ambient condition at $\sim 40^\circ\text{C}$. We recorded the photovoltaic metrics every 24 h. The encapsulated devices were under the open-circuit condition without an ultraviolet filter. At the first 200 h of the photostability test, the devices showed no evidence of degradation and then gradually decreased to 90% of their initial PCE after another 140 h.^{51,52}

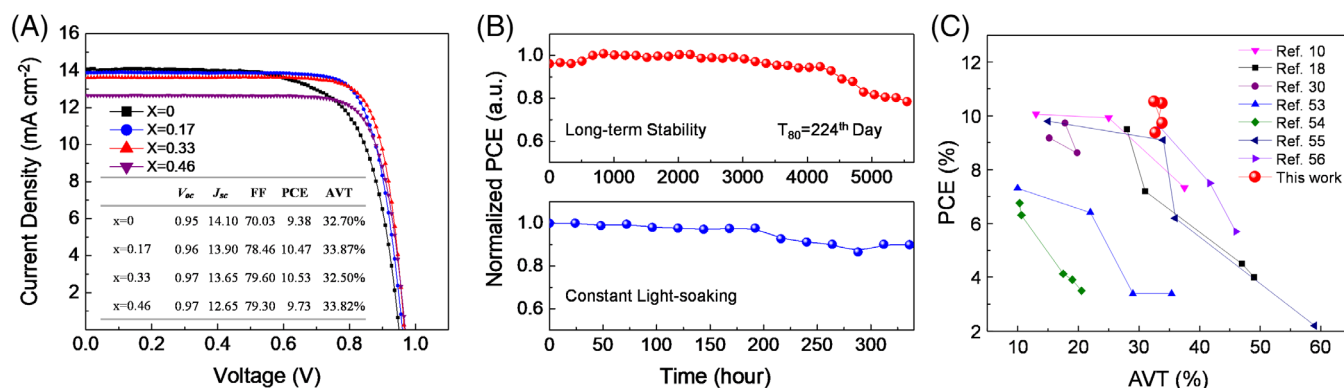


FIGURE 5 (A) J - V characteristics of ST-PSCs based on MEIS with different Br incorporation. (B) The long-term stability for $\text{Cs}_{0.05}\text{FA}_{0.83}\text{MA}_{0.12}\text{PbBr}_{0.33}\text{I}_{2.67}$ based ST-PSCs, without encapsulation stored in a desiccator with humidity below 10%. The photostability tests under constant AM1.5G illumination for $\text{Cs}_{0.05}\text{FA}_{0.83}\text{MA}_{0.12}\text{PbBr}_{0.33}\text{I}_{2.67}$ based ST-PSCs with encapsulation. (C) Whole device AVT versus PCE plot of the state-of-the-art ST-PSCs

To evaluate the figure-of-merit of ST-PSCs, Earlier reported works and our results are presented in Figure 4D, and Table S4 for comparison.^{10,18,30,53-56} As it can be seen, our MEIS-based ST-PSCs shows the best performance to our best knowledge, which can be interpreted by the highest PA value (Table S4). This illustrates that the incorporation of our MEIS template is a practical approach toward highly visually transparent, efficient, and robust ST-PSCs.

3 | CONCLUSION

In conclusion, we demonstrate MEIS for highly efficient, robust ST-PSCs with an optimal combination of AVT, PCE, and near-neutral color. The incorporation of MEIS combines versatile merits, such as light-trapping and benefiting the carrier collection at the interface. The alteration of the absorption spectra of perovskites based on MEIS resulted in the significantly enhanced J_{sc} without sacrificing the AVT, as well as a modification of desired near color neutrality. Additionally, the ST-PSCs exhibited appealing resistance against moisture and solar irradiation after engineering the halide blend ratio in perovskites.

3.1 | Experimental section

3.1.1 | Materials

ITO-coated glass substrates were purchased from Zhuhai Kaivo Optoelectronic Technology Co., Ltd. The ITO target was purchased from Chinese Rare Metal Material Co., Ltd. The IZO target was purchased from Goodwill Metal. Tetrakis(dimethylamino)tin (TDMASn, ≥ 5 N) was purchased from Hefei ADChem Semi-Tech.LTD. Methylammonium iodide (MAI), methylammonium bromide (MABr), and formamidinium iodide (FAI) were purchased from Dyesol. CsI was purchased from Shanghai Aladdin Bio-chem Technology Co. LTD. PbI_2 , $PbBr_2$, MoO_3 , lithium bis-(trifluoromethylsulfonyl)imide, 4-tert-butylpyridine were purchased from Sigma-Aldrich. Polystyrene colloidal suspensions (diameter = $1.01 \mu m$, SD = $0.03 \mu m$) were purchased from microParticles GmbH. All materials were used as received.

3.1.2 | Fabrication of SnO_2 /MEIS-ITO

The ITO glass was ultrasonically cleaned by detergent, acetone, isopropanol, and deionized water in sequence after blow-drying the substrate with N_2 .

The monodispersed polystyrene solution was prepared by mixing polystyrene colloidal suspensions, ethanol, and phosphoric acid at the ratio of 1:3:1 (vol%: vol%: vol%) followed by 15 min supersonic dispersion. Next, the as-prepared solution was steadily injected on a clean silicon wafer via a syringe pump. And then PS spheres slowly distributed on the top surface of DI water. Notably, a monolayer of the PS spheres floating on water was acquired. Therefore, it was necessary to gently and gradually slide the PS spheres on the top surface of DI water to prevent PS spheres from sinking. After putting it to stand for 3 h, sodium dodecyl sulfate (100 μl) was dropped into the container to form closely packed and well-ordered PS spheres. Thereafter, the water level was gradually reduced by utilizing the siphoning effect, and the PS spheres were transferred to the ITO glass. After that, the PS spheres coated ITO glass was dried in ambient conditions for 6 h. To alter the diameter of the PS spheres, the oxygen plasma treatment (at the power of 30 W, with the oxygen flow of 30 s.c.c.m.) was carried out.

The highly ordered PS spheres were filled by sputter deposition of 250 nm thick ITO at a deposition rate of 0.6 \AA s^{-1} . The D.C. sputtering uses an ITO target and a gas flow rate of 0.5 O_2 and 50 s.c.c.m Ar. Afterward, PS spheres were removed by soaking the sample in chloroform ultrasonic for 15 min, followed by ultrasonic cleaning by acetone for 5 min.

3.1.3 | ALD Depositions of ETL

SnO_2 was deposited by the ALD method (MNT Micro and Nanotech Co., Ltd) using TDMASn and DI water as precursors. The TDMASn, DI water sources were kept at $80^\circ C$ and room temperature, respectively. The deposition was carried out at $150^\circ C$. Each cycle consisted of Sn pulse (30 ms), Ar purge (30 s), H_2O pulse (300 ms), and Ar purge (30 s). The growth rate of the SiO_2 per cycle under this deposition condition was found to be 0.095-0.1 nm, which was estimated by SEM studies. In the present work, 200 cycles were run to yield 20 nm thick (actual thickness was between 18 and 22 nm). After that, the as-deposited SnO_2 was annealed at $400^\circ C$ in the air for 4 h, and then furnace cooling. To enhance the perovskite precursor solution's wettability on the as-grown sample, the oxygen plasma treatment (at the power of 30 W, oxygen flow of 30 s.c.c.m.) for 10 min was applied.

3.1.4 | Depositions of perovskites

The $Cs_{0.05}FA_{0.83}MA_{0.12}PbBr_{0.33}I_{2.67}$ was spin-coated from a precursor solution containing FAI(0.99 M), PbI_2 (1 M),

PbBr₂(0.2 M), CsI(0.06 M), and MAI(0.15 M) in a mixed solution of dimethylformamide: dimethyl sulfoxide 4:1 (vol%:vol%). The recipes of the Cs_{0.05}FA_{0.83}MA_{0.12}PbBr_xI_{3-x} precursor solution with different Br concentrations are listed in Table S6. The precursor solution was stirred at 1000 rpm in the N₂ filled glovebox at room temperature for exactly 2 h. Then 60 μl precursor solution was spin-coated on as-grown substrates with 1500 rpm for 5 s. Then spin rate was accelerated up to 5500 rpm for another 30 s. Antisolvent chlorobenzene (60 μl) was dropped at the 30th second. After the spin-coating of the precursor solution, the substrates were transferred to a hot plate and heated at 100 ± 5 °C for 20 min. The spin coating and annealing process were operated in the N₂ filled glovebox.

3.1.5 | HTL and Top-contact depositions

The HTM precursor solution was prepared by dissolving 80 mg spiro-OMeTAD in chlorobenzene (1 ml) and 4-tert-butylpyridine (28.8 μl) and Li salt solution (520 mg ml⁻¹ lithium bis-(trifluoromethylsulfonyl)imide in acetonitrile, 17.5 μl) was then added. The solution was spin-coated on the perovskite films with 3500 rpm for the 30 s. The films were left in a dry desiccator for 4 h. To protect the spiro-OMeTAD from sputtering damage, a buffer layer of 5 nm of MoO₃ was thermally evaporated at a rate of 1 Å s⁻¹ on the HTM layer before IZO deposition. The evaporation was operated in an evaporator that connected with the N₂ filled glovebox. Finally, 100 nm IZO was sputtered as a transparent electrode under a pressure of 8.2 × 10⁻² Pa of Ar at 50 W at the rate of 2 nm min⁻¹ at room temperature.

3.1.6 | Encapsulation

Devices were encapsulated in a nitrogen-filled glove box. The epoxy resin was dropped over the top electrode, and a small glass coverslip was placed on top. And then, the sample was exposed to ultraviolet illumination for 15 min.

3.1.7 | Characterization

The as-grown perovskites were characterized by the X-ray diffraction (XRD) (Bruker D8 X-ray Diffractometer, United States) utilizing Cu-Kα radiation and scanning electron microscopy (FESEM, JEOL JSM-7100F, Tescan VEGA3). Ultraviolet-visible spectroscopy (Varian Cary 500) was used to obtain the absorption and transmission spectra. The UV-vis Spectrophotometer-Perkin Elmer (Model: Lambda 20) was used to measure the absorbance

spectra. The Ocean Optics spectrometer (Model: FLAME-T-VIS-NIR-ES) obtained the color coordinate on the CIE *xy* 1931 chromaticity diagram. Photoluminescence (PL) and time-resolved photoluminescence (TRPL) were measured with an FS5 fluorescence spectrometer. Carrier lifetime was determined by mono-exponential decay fittings. The device performance was measured with an AM© solar simulator (Abet Class AAB Sun 2000, calibrated by a KG5-filtered Si reference cell). The current density-voltage (*J-V*) curves were measured with a Keithley 2400 under simulated AM1.5G illumination from a calibrated solar simulator with an irradiation intensity of 100 mW cm⁻². Ultraviolet photoelectron spectroscopy (UPS) was performed with Axis Ultra DLD multi-technique surface analysis system. The complex refractive index was measured with an ellipsometer (Model: Alpha—SE). To calculate the EQE, the photocurrent under monochromatic illuminations at different wavelengths was measured using a 150 W xenon lamp and a monochromator.

3.1.8 | FDTD simulations

FDTD method was conducted to study the absorption properties of the devices based on MEIS and planar counterpart. Plane-wave light source with a wavelength from 300 to 800 nm was normally illuminated onto the simulated structures. Periodic boundary condition was imposed at vertical boundaries, and only one unit cell was simulated to reduce the computational demand. The optical constants for ITO and SnO₂ were taken from the website refractiveindex.info. The complex refractive index of Cs_{0.05}FA_{0.83}MA_{0.12}PbBr_{0.33}I_{2.67} was calculated from the ellipsometer measurement in this work. We calculated the generation rate profile, namely, generated electron-hole pairs per unit volume per second $G_{\text{opt}}(\vec{r}, \lambda)$ using $G_{\text{opt}}(\vec{r}, \lambda) = \frac{k|E(\vec{r}, \lambda)|^2}{2h}$ where k is the imaginary part of the permittivity and $E(\vec{r}, \lambda)$ is the electric field.

ACKNOWLEDGMENTS

This work was supported by the National Natural Science Foundation of China (Project No. 51672231), the Science and Technology Plan of Shenzhen (Project Nos. JCYJ20170818114107730, JCYJ20180306174923335), the General Research Fund (Project Nos. 16309018, 16214619) from the Hong Kong Research Grant Council. Guangdong-Hong Kong-Macao Intelligent Micro-Nano Optoelectronic Technology Joint Laboratory (Project No. 2020B1212030010), HKUST Fund of Nanhai (Grant No. FSNH-18FYTRI01). The authors also acknowledge the support from the Center for 1D/2D Quantum Materials and the State Key Laboratory of Advanced Displays

and Optoelectronics Technologies at HKUST and Foshan Innovative and Entrepreneurial Research Team Program (2018IT100031). Yiyi Zhu and Lei Shu contributed equally to this work.

CONFLICT OF INTEREST

The authors declare no conflict of interest.

ORCID

Zhiyong Fan  <https://orcid.org/0000-0002-5397-0129>

REFERENCES

- Tai Q, Yan F. Emerging semitransparent solar cells: materials and device design. *Adv Mater.* 2017;29(34):1700192.
- File M. *Commercial Buildings Energy Consumption Survey (CBECS)*; Washington, DC: U.S. Department of Energy; 2015.
- Gagnon P, Margolis R, Phillips C. Rooftop photovoltaic technical potential in the United States of America; National Renewable Energy Laboratory-Data (NREL-DATA); 2019. <https://www.nrel.gov/docs/fy16osti/65298.pdf>
- 2015 Residential Energy Consumption Survey (RECS) Data, US Energy Information Administration; 2015. <https://www.eia.gov/consumption/residential/data/2015/>
- National renewable energy laboratory, best research cell efficiencies chart. <https://www.nrel.gov/pv/cell-efficiency.html>.
- Zhu Y, Shu L, Fan Z. Recent progress on semi-transparent perovskite solar cell for building-integrated photovoltaics. *Chem Res Chin Univ.* 2020;36(3):366-376.
- Drolet N Organic photovoltaic: efficiency and lifetime challenges for commercial viability. Paper presented at: 2012 MRS Spring Meeting & Exhibit, Moscone West Convention Center, Marriott Marquis, San Francisco, CA; 2012.
- You P, Liu Z, Tai Q, Liu S, Yan F. Efficient semitransparent perovskite solar cells with graphene electrodes. *Adv Mater.* 2015;27(24):3632-3638.
- Ono LK, Wang S, Kato Y, Raga SR, Qi Y. Fabrication of semi-transparent perovskite films with centimeter-scale superior uniformity by the hybrid deposition method. *Energ Environ Sci.* 2014;7(12):3989-3993.
- Jung JW, Chueh CC, Jen AKY. High-performance semitransparent perovskite solar cells with 10% power conversion efficiency and 25% average visible transmittance based on transparent CuSCN as the hole-transporting material. *Adv Energy Mater.* 2015;5(17):1500486.
- Guo F, Azimi H, Hou Y, et al. High-performance semitransparent perovskite solar cells with solution-processed silver nanowires as top electrodes. *Nanoscale.* 2015;7(5):1642-1649.
- Heo JH, Han HJ, Lee M, Song M, Kim DH, Im SH. Stable semi-transparent CH₃NH₃ PbI₃ planar sandwich solar cells. *Energ Environ Sci.* 2015;8(10):2922-2927.
- Quiroz COR, Levchuk I, Bronnbauer C, Salvador M, Forberich K, Heumüller T. Pushing efficiency limits for semitransparent perovskite solar cells. *J Mater Chem A.* 2015;3(47):24071-24081.
- Zhang H, Zhang Y, Yang G, Ren Z, Wei Y, Dong S. Vacuum-free fabrication of high-performance semitransparent perovskite solar cells via e-glue assisted lamination process. *Sci China Chem.* 2019; 62(7):875-882.
- Zhang Y, Wu Z, Li P, Ono LK, Qi Y, Zhou J. Fully solution-processed TCO-free semitransparent perovskite solar cells for tandem and flexible applications. *Adv Energy Mater.* 2018;8(1):1701569.
- Eperon GE, Burlakov VM, Goriely A, Snaith HJ. Neutral color semitransparent microstructured perovskite solar cells. *ACS Nano.* 2013;8(1):591-598.
- Eperon GE, Bryant D, Troughton J, Stranks SD, Johnston MB, Watson T. Efficient, semitransparent neutral-colored solar cells based on microstructured formamidinium lead trihalide perovskite. *J Phys Chem Lett.* 2015;6(1):129-138.
- Hörantner MT, Zhang W, Saliba M, Wojciechowski K, Snaith HJ. Templated microstructural growth of perovskite thin films via colloidal monolayer lithography. *Energ Environ Sci.* 2015;8(7):2041-2047.
- Ingram AL, Parker AR. A review of the diversity and evolution of photonic structures in butterflies, incorporating the work of John Huxley (The Natural History Museum, London from 1961 to 1990). *Philos Trans R Soc B Biol Sci.* 2008;363(1502):2465-2480.
- Vukusic P, Sambles JR. Photonic structures in biology. *Nature.* 2003;424(6950):852-855.
- Parker AR. Natural photonics for industrial inspiration. *Philos Trans R Soc A Math Phys Eng Sci.* 1894;2009(367):1759-1782.
- Yoshioka S, Kinoshita S. Effect of macroscopic structure in iridescent color of the peacock feathers. *FORMA-Tokyo.* 2002;17(2):169-181.
- Clausen J, Christiansen AB, Garnæs J, Mortensen NA, Kristensen A. Color effects from scattering on random surface structures in dielectrics. *Opt Express.* 2012;20(4):4376-4381.
- Huang YF, Chattopadhyay S, Jen YJ, Peng CY, Liu TA, Hsu KY. Improved broadband and quasi-omnidirectional anti-reflection properties with biomimetic silicon nanostructures. *Nat Nanotechnol.* 2007;2(12):770-774.
- Shalin AS. Broadband blooming of a medium modified by an incorporated layer of nanocavities. *JETP Lett.* 2010;91(12):636-642.
- Leung SF, Gu L, Zhang Q, Tsui KH, Shieh JM, Shen CH. Roll-to-roll fabrication of large scale and regular arrays of three-dimensional nanospikes for high efficiency and flexible photovoltaics. *Sci Rep.* 2014;4(1):1-8.
- Shalin AS. Optical antireflection of a medium by nanostructural layers. *Prog Electromagn Res.* 2011;31:45-66.
- Glaser T, Ihring A, Morgenroth W, Seifert N, Schröter S, Baier V. High temperature resistant antireflective moth-eye structures for infrared radiation sensors. *Microsyst Technol.* 2005;11(2-3):86-90.
- Shalin AS, Nikitov SA. Approximate model for universal broadband antireflection nano-structure. *Prog Electromagn Res.* 2013; 47:127-144.
- Kim GM, Tatsuma T. Semi-transparent perovskite solar cells developed by considering human luminosity function. *Sci Rep.* 2017;7(1):10699.
- Zheng X, Wei Z, Chen H, Zhang Q, He H, Xiao S. Designing nanobowl arrays of mesoporous TiO₂ as an alternative electron transporting layer for carbon cathode-based perovskite solar cells. *Nanoscale.* 2016;8(12):6393-6402.
- Sahli F, Werner J, Kamino BA, Bräuninger M, Monnard R, Paviet-Salomon B. Fully textured monolithic perovskite/silicon tandem solar cells with 25.2% power conversion efficiency. *Nat Mater.* 2018;17(9):820-826.

33. Kang SM, Jang S, Lee JK, Yoon J, Yoo DE, Lee JW. Moth-eye TiO₂ layer for improving light harvesting efficiency in perovskite solar cells. *Small*. 2016;12(18):2443-2449.
34. Zhu Y, Poddar S, Shu L, Fu Y, Fan Z. Recent progress on interface engineering for high-performance, stable perovskites solar cells. *Adv Mater Interfaces*. 2020;7(11):2000118.
35. Tavakoli MM, Zakeeruddin SM, Grätzel M, Fan Z. Large-grain tin-rich perovskite films for efficient solar cells via metal alloying technique. *Adv Mater*. 2018;30(11):1705998.
36. Sutton RJ, Eperon GE, Miranda L, Parrott ES, Kamino BA, Patel JB. Bandgap-tunable cesium lead halide perovskites with high thermal stability for efficient solar cells. *Adv Energy Mater*. 2016;6(8):1502458.
37. Stranks SD, Eperon GE, Grancini G, Menelaou C, Alcocer MJ, Leijtens T. Electron-hole diffusion lengths exceeding 1 micrometer in an organometal trihalide perovskite absorber. *Science*. 2013;342(6156):341-344.
38. Di J, Chang J, Liu S. Recent progress of two-dimensional lead halide perovskite single crystals: crystal growth, physical properties, and device applications. *EcoMat*. 2020;2(3):e12036.
39. Judd DB. *Contributions to Color Science*. Vol 545. Gaithersburg, MA: Department of Commerce, National Bureau of Standards; 1979.
40. Zhang F, Yang B, Mao X, Yang R, Jiang L, Li Y. Perovskite CH₃NH₃PbI_{3-x}Br_x single crystals with charge-carrier lifetimes exceeding 260 μs. *ACS Appl Mater Interfaces*. 2017;9(17):14827-14832.
41. Huang H, Lu L, Wang J, Yang J, Leung SF, Wang Y. Performance enhancement of thin-film amorphous silicon solar cells with low cost nanodent plasmonic substrates. *Energ Environ Sci*. 2013;6(10):2965-2971.
42. Lin Y, Xu Z, Yu D, Lu L, Yin M, Tavakoli MM. Dual-layer nanostructured flexible thin-film amorphous silicon solar cells with enhanced light harvesting and photoelectric conversion efficiency. *ACS Appl Mater Interfaces*. 2016;8(17):10929-10936.
43. Hua B, Lin Q, Zhang Q, Fan Z. Efficient photon management with nanostructures for photovoltaics. *Nanoscale*. 2013;5(15):6627-6640.
44. Brongersma ML, Cui Y, Fan S. Light management for photovoltaics using high-index nanostructures. *Nat Mater*. 2014;13(5):451-460.
45. Kam M, Zhu Y, Zhang D, Gu L, Chen J, Fan Z. Efficient mixed-cation mixed-halide perovskite solar cells by all-vacuum sequential deposition using metal oxide electron transport layer. *Solar RRL*. 2019;3(7):1900050.
46. Bi D, Tress W, Dar MI, Gao P, Luo J, Renevier C. Efficient luminescent solar cells based on tailored mixed-cation perovskites. *Sci Adv*. 2016;2(1):e1501170.
47. Kim HJ, Seo KW, Noh YJ, Na SI, Sohn A, Kim DW. Work function and interface control of amorphous IZO electrodes by MoO₃ layer grading for organic solar cells. *Sol Energy Mater Sol Cells*. 2015;141:194-202.
48. Lin QF, Sarkar D, Yeung M, Blankemeier L, Hazra J. Scalable indium phosphide thin-film nanophotonics platform for photovoltaic and photoelectrochemical devices. *ACS Nano*. 2017;11(5):5113-5119.
49. Yu R, Ching KL, Lin Q, Leung SF, Arcrossito D, Fan Z. Strong light absorption of self-organized 3-D nanopike arrays for photovoltaic applications. *ACS Nano*. 2011;5(11):9291-9298.
50. Tavakoli MM, Lin Q, Leung SF, Lui GC, Lu H, Li L. Efficient, flexible and mechanically robust perovskite solar cells on inverted nanocone plastic substrates. *Nanoscale*. 2016;8(7):4276-4283.
51. Kundu S, Kelly TL. In situ studies of the degradation mechanisms of perovskite solar cells. *EcoMat*. 2020;2(2):e12025.
52. Tai Q, Cao J, Wang T, Yan F. Recent advances toward efficient and stable tin-based perovskite solar cells. *EcoMat*. 2019;1(1):e12004.
53. Roldán-Carmona C, Malinkiewicz O, Betancur R, Longo G, Momblona C, Jaramillo F. High efficiency single-junction semitransparent perovskite solar cells. *Energy Environ Sci*. 2014;7(9):2968-2973.
54. Upama MB, Mahmud MA, Yi H, Elumalai NK, Conibeer G, Wang D. Low-temperature processed efficient and colourful semitransparent perovskite solar cells for building integration and tandem applications. *Org Electron*. 2019;65(1):401-411.
55. Zhang L, Hörantner MT, Zhang W, Yan Q, Snaith HJ. Near-neutral-colored semitransparent perovskite films using a combination of colloidal self-assembly and plasma etching. *Sol Energy Mater Sol Cells*. 2017;160:193-202.
56. Kwon HC, Kim A, Lee H, Lee D, Jeong S, Moon J. Parallelized nanopillar perovskites for semitransparent solar cells using an anodized aluminum oxide scaffold. *Adv Energy Mater*. 2016;6(20):1601055.

SUPPORTING INFORMATION

Additional supporting information may be found online in the Supporting Information section at the end of this article.

How to cite this article: Zhu Y, Shu L, Zhang Q, et al. Moth eye-inspired highly efficient, robust, and neutral-colored semitransparent perovskite solar cells for building-integrated photovoltaics. *EcoMat*. 2021;1-11. <https://doi.org/10.1002/eom2.12117>